galaxies

MDPI

Article

M 1-92: The Death of an AGB Star Told by Its Isotopic Ratios

Elisa Masa [1,*], Javier Alcolea [1], Miguel Santander-García [1], Valentín Bujarrabal [2], Carmen Sánchez Contreras [3] and Arancha Castro-Carrizo [4]

[1] Observatorio Astronómico Nacional (IGN), Alfonso XII 3, E-28014 Madrid, Spain; j.alcolea@oan.es (J.A.); m.santander@oan.es (M.S.-G.)
[2] Observatorio Astronómico Nacional (IGN), Ap 112, E-28803 Alcalá de Henares, Spain; v.bujarrabal@oan.es
[3] Centro de Astrobiología (CSIC-INTA), Camino Bajo del Castillo s/n, E-28691 Villanueva de la Cañada, Spain; csanchez@cab.inta-csic.es
[4] Institute de Radioastronomie Millimetrique, rue de la Piscine 300, F-38406 St. Martin d'Heres, France; ccarrizo@iram.fr
* Correspondence: e.masa@oan.es

Abstract: Ongoing improvements in the sensitivity of sub-mm- and mm-range interferometers and single-dish radio telescopes allow for the increasingly detailed study of AGB and post-AGB objects in molecular species other than ^{12}CO and ^{13}CO. With a new update introduced in the modelling tool SHAPE + shapemol, we can now create morpho-kinematical models to reproduce observations of these AGB and post-AGB circumstellar shells in different molecular species, allowing for an accurate description of their physical features as well as their molecular abundances and isotopic ratios. The pre-planetary nebula M1-92 (Minkowski's Footprint) is one of the most complex objects of this kind, with a wide range of physical conditions and more than 20 molecular species detected. We model this nebula, reproducing the observational data from IRAM-30m and HSO/HiFi spectra and NOEMA interferometric maps, trying to understand the unusual evolution of its central star in the last phases of its life. The results show interesting features that tell us the story of its death. According to standard evolution models, a ^{17}O/^{18}O isotopic ratio of 1.6 implies a stellar initial mass of $\sim 1.7 M_{\odot}$. Such a star should have turned C-rich by the end of the AGB phase, in striking contrast to the O-rich nature of the nebula. The most plausible way of reconciling this discrepancy is that M1-92 resulted from a sudden massive ejection event, interrupting the AGB evolution of the central source and preventing its transformation into a C-rich star. We also detect a changing ^{12}C/^{13}C ratio across the nebula, which is particularly relevant in the inner equatorial region traced by HCO^{+} and H^{13}CO^{+}, indicating an isotopic ratio variation taking place at some point during the last 1200 yr.

Keywords: AGB evolution; post-AGB evolution; planetary nebulae; pre-planetary nebulae; PN M 1-92; post-AGB stars; planetary nebulae shaping; chemical abundances; elemental isotopic ratios; molecular line observations; mm-wave interferometry

check for updates

Citation: Masa, E.; Alcolea, J.; Santander-García, M.; Bujarrabal, V.; Sánchez Contreras, C.; Castro-Carrizo, A. M 1-92: The Death of an AGB Star Told by Its Isotopic Ratios. *Galaxies* **2024**, *12*, 63. https://doi.org/10.3390/galaxies12050063

Academic Editor: Milan S. Dimitrijević

Received: 6 September 2024
Revised: 2 October 2024
Accepted: 8 October 2024
Published: 10 October 2024

1. Introduction

The morphological variety displayed by planetary nebulae (PNe) is one of the aspects of stellar evolution that still defies our comprehension. The processes of mass ejection that reshape the isotropic circumstellar envelopes (CSEs) of asymptotic giant branch (AGB) stars into bipolar or multi-polar PNe are still a mystery for which several mechanisms have been proposed [1–3], most of them requiring the presence of a companion to provide the angular momentum that results in an ejection through a preferential axis [4].

Pre-planetary nebulae (pPNe), the transitional objects in between AGB CSEs and PNe, are privileged sources of information on this morphological and kinematic transformation, as they allow us to study the first stages of the fast bipolar mass ejection that substitutes and impinges onto the slow spherical wind of AGB stars. During the pPNe stage, the nebula is still rich in molecular gas, an excellent environment for working with rotational lines of many species, both by using connected mm-interferometry to obtain high spectral and spatial resolution maps and single-dish line profiles. Depending on the studied molecule, we can also trace some dynamic events, such as wind shocks and ionisation fronts. A combination of a few of these maps and line profiles across different molecules can provide a full description of the nebula's properties (excitation conditions, densities, temperatures, molecular abundances, etc.). Therefore, its internal structures and kinematics are also revealed, leading to valuable conclusions regarding key variables of this transformation process, from the internal dynamics to isotopic ratios, also adding significant constraints to the shaping mechanisms responsible for the AGB CSEs to PNe transformation and the AGB and post-AGB evolution of these stars (e.g., [5]).

Minkowsky's Footprint, pPN M1-92, is a particularly interesting nebula in this context. Located at a distance of 2.5 kpc around a B-type post-AGB star, it shows a bipolar shape $11'' \times 6''$ in size [6]. Previous mapping of the ^{13}CO $J = 2 - 1$ line emission at 0.5 arc-sec resolution showed that the main nebular structure has a constant radial velocity gradient of 7.4 km s^{-1} per arc-sec [1,7].

In Figure 1 we can see a representation of our best-fit model of the nebula, which is divided into different structures, some of them reported in previous works (components 1 + 2, 3 + 4, 5, and 6) and some proposed in this study (division between components 1 and 2 and 3 and 4). With this, the nebula consists of two emptied lobes (component 6), divided by an equatorial denser structure (components 3 and 4), which end in two axial tips (components 1 and 2). All these components show a homologous expansion with a kinematical age of 1200 yr. This suggests that M1-92 resulted from a brief mass-loss event amounting to $\sim$0.9 $M_\odot$ in less than 100 yr, resulting in a mass loss rate larger than 10^{-2} $M_\odot$ yr^{-1}[8]. This imposes strong constraints to the mechanism powering these ejections and the shaping of the nebula, in line with those provided by common envelope ejection models [9,10].

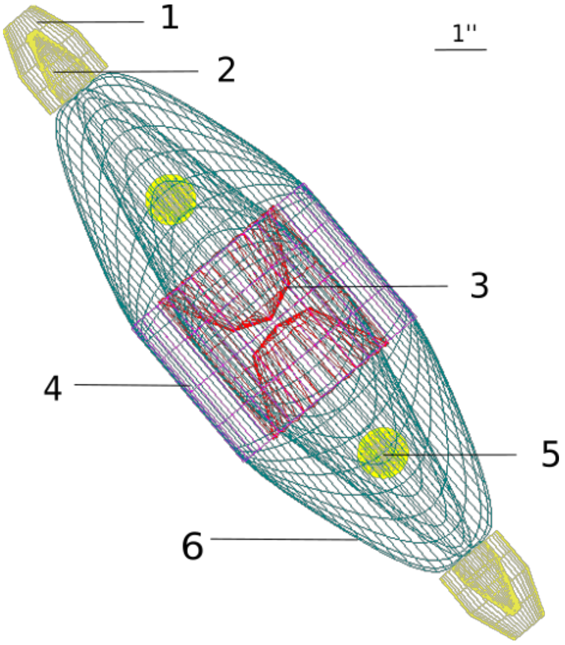

Figure 1. Wired representation of the best-fit model based on available data of the molecular envelope of the pPN M1-92 showing its structures, together with a scale to show the distance of 1″ (equivalent to 3.75×10^{16} cm at the nebula's location). 1: (Yellow) Outer layer of the tips structure, continuation of the main shell (6) with very similar conditions. 2: (Yellow) Inner layer of the tips, with hotter gas. 3: (Red) Equatorial structure with high density, defining the lobes' base. 4: (Purple) Ring around the central cylinder with the same physical properties as the main shell. 5: (Bright yellow) Knots inside the empty lobes where ionised gas has been found. 6: (Green) The main shell, which forms the walls of the empty lobes and mainly consists of cold gas.

In addition, two compact regions inside the lobes, the knots (component 5 in Figure 1), have been revealed by the emission from optical atomic forbidden lines and infrared vibrationally excited H_2 line, and are thought to contain shocked gas [11,12]. These areas present younger kinematic ages (about 650 yr [13]) than the main shell mapped by CO. It is worth noting that, contrary to other sources [14,15], no proof of an older spherical AGB CSE has been found around the object, which suggests that at least the main parts of the nebula itself is the CSE ejected during a massive mass loss event.

This object also presents interesting chemistry and elemental isotopic ratios. It has more than 20 molecular species detected by single dish observations including all CO stable isotopomers, HCN, $H^{13}CN$, HCO^+, and $H^{13}CO^+$ [16]. Isotopic ratios for $^{12}C/^{13}C$ as well as $^{17}O/^{18}O$ have been studied, suggesting that despite the O-rich nature of the nebula, the central AGB star should have turned C-rich, had the sudden mass-loss event occurred later [7,8,17] or followed the usual evolution of AGB stars under the assumption of solar-like metallicity.

2. Observational Data and Modelling Process

Although M1-92 has been modelled before with different software [8,17] this time a new model was created from scratch using `SHAPE`. `SHAPE` is a free software that allows for 3-D modelling and simulation of the emission of extended, gaseous astrophysical objects [18]. However, it was not originally intended to simulate emission from molecular lines. This is done through `shapemol`, a built-in plugin until now limited to lines from ^{12}CO and ^{13}CO [19]. As part of this project, we have increased `shapemol` capabilities by including $C^{17}O$, $C^{18}O$, and HCN and HCO^+ and their ^{13}C substitutions. The basis of these computations are the Large Velocity Gradient (LVG) [20] approximation treatment of the non-LTE excitation of the species, and an exact solution for the radiative transfer and simulation of the emerging line emission as observed either with single dishes or interferometers. Further details on these computations and the results presented here will be discussed by Masa et al. (in prep.).

The observational data we aim to reproduce with our model comes from eight species: ^{12}CO, ^{13}CO, $C^{17}O$, $C^{18}O$, HCN, $H^{13}CN$, HCO^+, and $H^{13}CO^+$. We work with both single-dish line profiles and interferometric maps. In total 23 line profiles and five interferometric maps were reproduced by our model, although only 17 will be discussed as HCO^+ and HCN provide similar results. We have single-dish data for five lines ($J = 1 - 0$, $J = 2 - 1$, $J = 5 - 4$, $J = 7 - 6$, and $J = 9 - 8$) from ^{12}CO, two lines ($J = 1 - 0$ and $J = 2 - 1$) from ^{13}CO, $C^{17}O$, and $C^{18}O$, and three lines ($J = 1 - 0$, $J = 2 - 1$, and $J = 3 - 2$) for HCN, $H^{13}CN$, HCO^+, and $H^{13}CO^+$. In addition, the five species with interferometric maps were ^{13}CO, $C^{17}O$, $C^{18}O$, HCN, and HCO^+, all of them mapped in the $J = 2 - 1$ line. All maps come from IRAM's interferometer, NOEMA, while most of the single-dish lines come from IRAM-30m, except for the ^{12}CO $J = 5 - 4$, $J = 7 - 6$, and $J = 9 - 8$ that were obtained through Herschel Space Observatory (HSO) HIFI observations. Table 1 summarises the conditions under which the data was taken.

Table 1. Observational data information.

Transition	Telescope	Observation Date	HPBW
^{12}CO $J = 1 - 0$ [2,3]	IRAM 30m RMT	Sept. 2015 Feb., May, Jun. 2016	21.5″
^{12}CO $J = 2 - 1$ [1,2,3]	IRAM 30m RMT	Jun., Jul. 2015 Sept. 2015 June 2016	10.7″
^{12}CO $J = 5 - 4$ [4]	HIFI/HSO	Nov. 2010	36.1″
^{12}CO $J = 7 - 6$ [5]	HIFI/HSO	Dec. 2012	25.8″

Table 1. *Cont.*

Transition	Telescope	Observation Date	HPBW
^{12}CO $J = 9 - 8$ [4]	HIFI/HSO	May 2011	20.1″
^{13}CO $J = 1 - 0$ [1,2,3]	IRAM 30m RMT	Jun., Jul. 2015 Sept. 2015 Feb., May, Jun. 2016	22.5″
^{13}CO $J = 2 - 1$ [3]	IRAM 30m RMT	Feb., May, Jun. 2016	11.2″
C^{17}O $J = 1 - 0$ [1,2,3]	IRAM 30m RMT	Jun., Jul. 2015 Sept. 2015 Feb., May, Jun. 2016	22.0″
C^{17}O $J = 2 - 1$ [2,3]	IRAM 30m RMT	Sept. 2015 Feb. 2016	11.0″
C^{18}O $J = 1 - 0$ [1,2,3]	IRAM 30m RMT	Jun., Jul. 2015 Sept. 2015 Feb., May, Jun. 2016	22.6″
C^{18}O $J = 2 - 1$ [3]	IRAM 30m RMT	Feb., Jun. 2016	11.3″
HCO^{+} $J = 1 - 0$ [2,3]	IRAM 30m RMT	Sept. 2015 Feb. 2016	27.8″
HCO^{+} $J = 2 - 1$ [3]	IRAM 30m RMT	May 2016	13.9″
HCO^{+} $J = 3 - 2$ [3]	IRAM 30m RMT	Feb., May 2016	9.3″
H^{13}CO^{+} $J = 1 - 0$ [3]	IRAM 30m RMT	Feb., May 2016	28.6
H^{13}CO^{+} $J = 2 - 1$ [3]	IRAM 30m RMT	May 2016	14.3″
H^{13}CO^{+} $J = 3 - 2$ [3]	IRAM 30m RMT	June 2016	9.5″
^{13}CO $J = 2 - 1$ [6]	NOEMA	Mar., Apr. 2018	0.76″× 0.51″ *
C^{17}O $J = 2 - 1$ [6]	NOEMA	Mar., Apr. 2018	0.76″× 0.51″ *
C^{18}O $J = 2 - 1$ [6]	NOEMA	Mar., Apr. 2018	0.76″× 0.51″ *
HCO^{+} $J = 2 - 1$ [6]	NOEMA	Mar., Apr. 2018	0.81″× 0.56″ **
H^{13}CO^{+} $J = 2 - 1$ [6]	NOEMA	Mar., Apr. 2018	0.81″× 0.56″ **

[1] Project 050-15. [2] Project 160-15. [3] Project 047-16. [4] Project GT1_dteyssie_1. [5] Project OT1_vbujarra_4. [6] Project W17BJ. * PA: 26°; MRS: 5.5″. ** PA: 35°; MRS: 10″.

The best-fit model to reproduce these observations is shown in Figure 1, where each of the structures previously described are represented. In some cases, like the polar tips or the equatorial region, a two-layered structure had to be incorporated to accurately reproduce the observational data. Using Figure 1 as a reference, our final model's physical properties are:

1. Outer tips: as a continuation of the main shell (6), they have very similar values for its variables: a cold temperature of 20 K and a relatively high density of 7×10^4 cm^{-3}.
2. Inner tips: made of warm (600 K) but very thin (7.5×10^3 cm^{-3}) gas, with 5 km s^{-1} of turbulence, a slightly higher value than the rest of the nebula.
3. Equatorial structure: it has a high density at the very centre (1.75×10^5 cm^{-3}) that decreases with radius with a linear dependence until 7×10^4 cm^{-3}. Similarly, in terms of temperature, we have warm gas at the centre (160 K) that decreases with radius in a multiplicative inverse law, until the 17 K of the shell are reached.
4. Ring: it is the area of the main shell that is located around the equatorial structure. Despite this differentiation, all its physical variables are the same as those of the shell. Its purpose in the model is to discriminate the spatial distribution of certain species across the equator, as some are present in the centre (equatorial structure) but not in the ring.

5. Knots: they represent the ionised gas found inside the lobes, with an assigned temperature of 500 K and a density of 3.5×10^4 cm^{-3}. These are the structures with the highest turbulence, 18 km s^{-1}, in addition to a velocity law similar to that of a shock front, where the head of the front has slowed down to 15 km s^{-1} while the rest is advancing at 55 km s^{-1}.
6. Shell: it is the main structure of the nebula, with a temperature of just 17 K and a constant density of 7×10^4 cm^{-3}. Like all other structures except for knots and the inner tips, its turbulence is set at 2 km s^{-1}.

The velocity law of the entire nebula, except for the knots in point 5, is set to a radial gradient of 7.5 km s^{-1}. The best-fit model is rendered with a resolution of 127 × 127 cells in a $40'' \times 40''$ window, using the observed sizes for the nebula and a beam the same size of observations for each spectral line. In addition, the resulting maps from the model are put through the same interferometric process (uv-filtering, uv-mapping, and cleaning) as that of real observations.

Finally, our model is considered finished only when it is able to simultaneously reproduce the observational data with changes between different species owing only to their different abundances with respect to H_2.

3. Results

3.1. CO Results

CO is the best molecule to trace the areas of cold but dense gas, which means it will perfectly define the limits of the outer shell of this nebula and show the overall structure of the oldest region. Thanks to the three maps of different CO isotopes we can reproduce the geometry and physical distribution of gas. In Figure 2, we present the comparison side by side between the observational data of the ^{13}CO map (the brightest CO isotopogue of the three mapped) and our model reproduction, together with the resulting residuals. In particular, these images consist of P-V diagrams, which due to the linear velocity law ($v \propto r$), we can use to plot "slices" of the nebula, since the observed velocity will always be proportional to the position along the line of sight in the structures following this law.

In the central image showing the reproduction from our model, we can identify features resulting from the instrumental processing of the observations due to uneven and incomplete coverage of the *uv*-plane as artefact emission around the spatial axis, as well as certain asymmetries across the nebula that are not present in our perfectly symmetrical model, like the narrower parts close to the polar tips or a slightly wavy texture on the external surface of the shell.

Finally, observing the resulting fluxes in the residues image, we can conclude that our model is a very accurate description of the part of the nebula traced by ^{13}CO except for a bright spot found on the central part of the nebula, slightly displaced towards positive velocities. The rest of the residual spots come from a lack of symmetry on the real nebula in comparison to our model, which makes it look like there is some offset between the two of them, despite having the same alignment.

It is important to notice that in these maps the lobes of the nebula appear to be empty, with no sign of the knots with ionised gas previously mentioned. Despite not being mapped in any CO species, the wide range of energies covered by the observational profiles shows an evolution from a single peak emission in the low-J lines to a three peak distribution, as seen in Figure 3. This can only be reproduced by adding a second layer of warmer gas inside the polar tips and with the presence of CO in the knots. Therefore, the lack of these structures in the CO maps is not due to lack of CO species in the ionised knots, but because of the low excitation gas preferentially traced by the mapped low-J transitions.

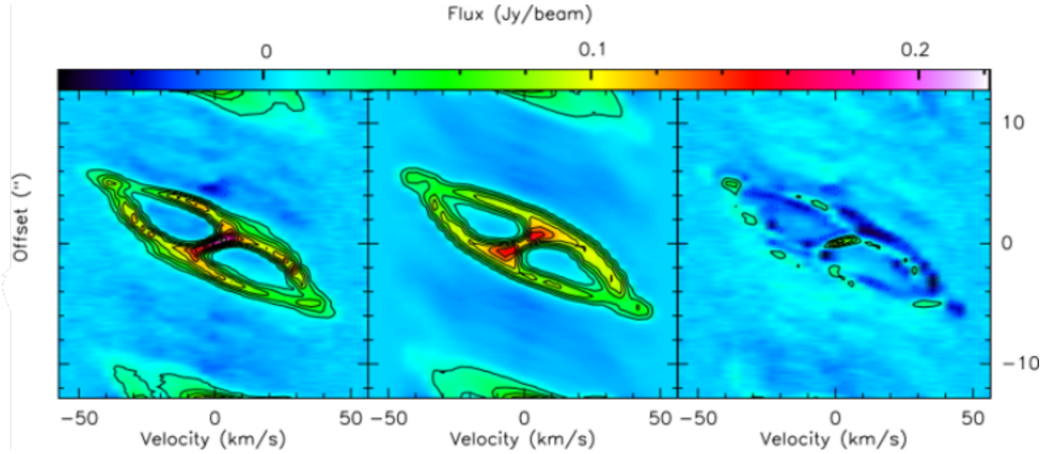

Figure 2. P-V diagrams along the nebular main symmetry axis for ^{13}CO maps $J = 2 - 1$ transition. Observational data is shown on the left, model reproduction on the central panel and residuals (observation-model) on the right.

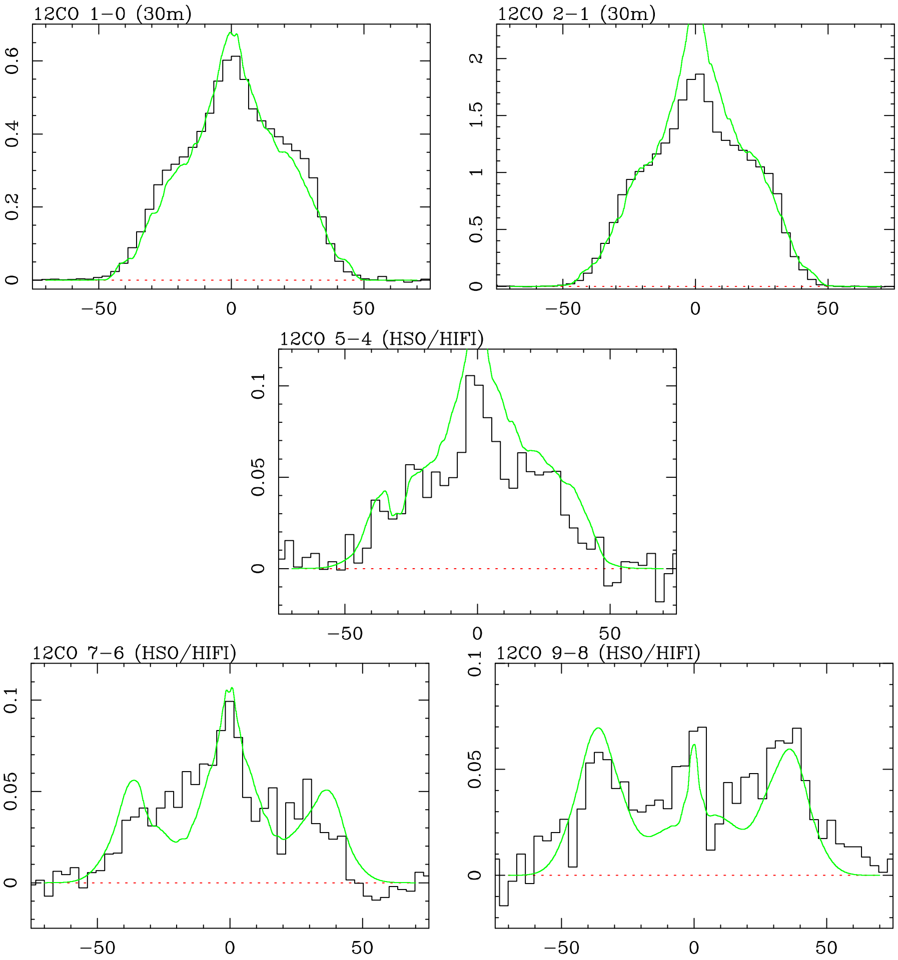

Figure 3. Line profiles of ^{12}CO. Observational data in black and model reproduction in green. All plots show main beam temperature (K) vs. LSR velocity (km s^{-1}).

Following this process for all the observational data collected from the four CO isotopes, we derive a specific value for the abundance relative to H_2 for each species, these being:

- ^{12}CO: 5.5×10^{-4};
- ^{13}CO: 1.8×10^{-5};

- $C^{17}O$: 1.0 × 10^{-6};
- $C^{18}O$: 6.0 × 10^{-7}.

With all values being constant across the nebula. With them we can derive the ratios between the different isotopes:

- $^{12}CO/^{13}CO/C^{17}O/C^{18}O = 1/30/550/880$;
- $C^{17}O/C^{18}O = 1.6$.

The ratios were obtained as a consequence of the adjustments needed in the relative abundance to reproduce the observational data by our model, but they match those obtained directly by line ratios after applying frequency and Einstein coefficient corrections in the case of the optically thin species ($C^{17}O$ and $C^{18}O$). Also, taking into account the noise in the observational data that our model reproduces, we can also derive error values for these ratios: 1.60 ± 0.05 for the $C^{17}O/C^{18}O$ ratio and 30 ± 2 for the $^{12}CO/^{13}CO$ ratio. However, due to the high co-dependence among all variables, it is not possible to derive a reliable error for the values of the physical variables obtained from our best-fit model, as observations do not provide a direct number to compare to as in the case of abundance ratios.

3.2. HCO^+ and HCN Results

Despite delineating the outer regions of the nebula, the observational data of CO and its isotopes still lack information on the spatial and velocity distribution of the warmer regions, particularly of the ionised knots. The velocity law set for these structures could only be deduced from HCO^+ and HCN maps. In Figure 4, we show the P-V diagrams from the HCO^+ maps, the one with the best signal-to-noise ratio, and compare the observational data with the model reproduction. This time we clearly see the knots in between the central region and the polar tips, with the emission centred in two velocity values. This distribution is accurately reproduced by the model when applying the velocity law of a shock front, as seen in the central panel. Once again, the residuals panel shows an excellent fit obtained by our model, except for the bright spot on the central region, again clearly displaced towards positive velocities.

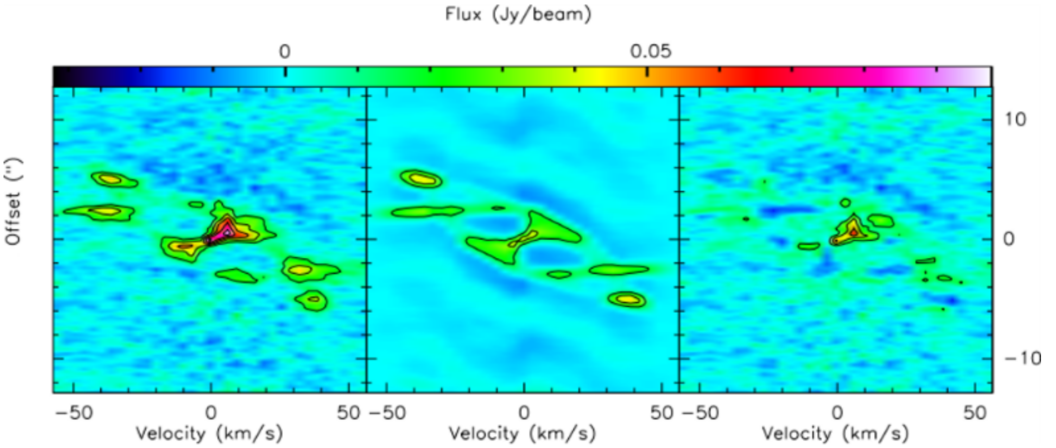

Figure 4. P-V diagrams along the nebular main symmetry axis for HCO^+ maps $J = 2 - 1$ transition. Observational data is shown on the left, model reproduction on the central panel and residuals (observation-model) on the right.

Following the same process we did with CO, we adjusted the line profiles of HCO^+, $H^{13}CO^+$, HCN, and $H^{13}CN$ to obtain relative abundances and isotopic ratios. Using the HCO^+ molecule as shown in Figure 5, this time different values of relative abundance are needed for each structure, being up to three order of magnitude higher in some inner regions than in the outer shell. We obtain the following relative abundances:

- Shell and outer tips: $HCO^+ = 5.00 \times 10^{-9}$; $H^{13}CO^+ = 5.00 \times 10^{-10}$;
- Ring: $HCO^+ = 2.50 \times 10^{-8}$; $H^{13}CO^+ = 2.50 \times 10^{-9}$;

- Centre: $HCO^+ = 1.00 \times 10^{-8}$; $H^{13}CO^+ = 1.00 \times 10^{-9}$;
- Knots: $HCO^+ = 1.75 \times 10^{-7}$; $H^{13}CO^+ = 1.75 \times 10^{-8}$;
- Inner tips: $HCO^+ = 1.60 \times 10^{-6}$; $H^{13}CO^+ = 1.60 \times 10^{-7}$.

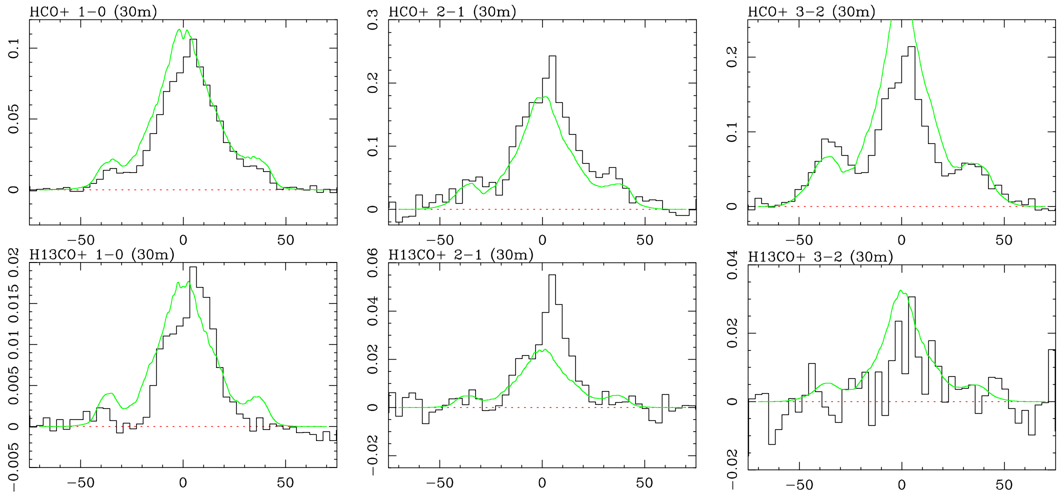

Figure 5. Line profiles of HCO^+ and $H^{13}CO^+$. Observational data in black and model reproduction in green. All plots show temperature of main beam (K) vs. velocity (km s^{-1}).

Comparing both isotopologues we derive an isotopic ratio of $HCO^+/H^{13}CO^+ = 10.0 \pm 0.3$. For $H^{13}CN$ the signal-to-noise ratio is too low for estimating this ratio, only allowing an upper limit for the isotopic ratio compatible with the one found for HCO^+.

4. Discussion and Conclusions

We have built a robust model for M1-92 that is able to reproduce observational data from several telescopes. This multi-species and multi-transition analysis allows us to study the physical and chemical properties of the nebula. All adjustments in both single-dish lines and interferometric maps are reproduced within a reasonable margin of accuracy, except for a bright spot found in the central area of the nebula. We have not attempted to reproduce it on this model as we lack information about its position, size, and velocity law, given the insufficient resolution reached by these maps.

The analysis of CO data and the derived relative abundances for $C^{17}O$ and $C^{18}O$ confirm a $^{17}O/^{18}O$ ratio of 1.6. Assuming a solar metallicity for the central star, which is a reasonable assumption given its location in the disk of our galaxy (galactic declination $\sim 4^\circ$), this ratio corresponds to an initial mass for the central AGB star of around $1.7M_\odot$ as seen in Figure 2 of De Nutte et al., 2017 [21], where all three models compared [22–24] agree on the results for that range. That mass should have been enough for the star to remain on the thermally pulsing AGB phase for long enough to become C-rich according to models and observations where stars with similar or lower initial mass that follow a standard AGB evolution to become C-rich [25–28]. In addition, we find that the $0.9M_\odot$ found for the nebula with homologous expansion is around 80% of the expected mass-loss of a $1.7M_\odot$ star during its entire AGB phase. The combination of this isotopic ratio information, together with a nebular age of 1200 yr from the kinematics for most of the mass, makes it evident that a common envelope ejection or a sudden event of similar characteristics is a must when explaining the origin and shaping of this nebula. This event, with such a huge mass ejection, would have been enough to interrupt the AGB phase, preventing the star from becoming C-rich and resulting in the final mixed chemistry we find on the nebula, thus providing a natural explanation for all the data gathered so far.

When modelling the nebula and its physical properties, we discover a new structure distribution on the polar tips that had never been studied before. The two layers of this region mean that gas with two very different physical properties almost coexists in very specific positions along the main axis. Given that the properties of the inner gas are very similar to those of the knots and both are found across the same axis, it is reasonable to assume this inner gas comes from a previous ejection with the same origin as the one that formed the knots. This is also supported by the discrepancy in the $^{12}C/^{13}C$ isotopic ratio found between different molecules. Despite this seemingly contradictory result, it is important to notice that CO and HCO^+ trace different regions with different conditions, while CO is dominated by the emission of dense and cold gas, especially the low-J lines, which are the ones used to derive isotopic ratios, HCO^+ trace the regions with active shocks, are turbulent, and with much higher temperatures despite their lower density. As a result, the two species probe the isotopic ratio in molecular gas with very different physical conditions, resulting in different values for each structure instead of contradictory information. This result can not be a consequence of opacity as CO has the higher $^{12}C/^{13}C$ ratio of both, plus these results are found through the values used for a multi-species modelling that includes these opacity effects.

Another relevant difference found between CO and HCO^+ is the profile shape and how its emission peak in both HCO^+ and $H^{13}CO^+$ is always dominated by that central spot that our model is unable to reproduce, as it is always displaced towards positive velocities. This feature, clearly seen in Figure 5, and its increased dominance in the $H^{13}CO^+$ lines suggest that not only the central bright spot has different physical properties than the rest of the equatorial region, but that it also has a $^{12}C/^{13}C$ ratio more in line with the results found by HCO^+ than those of CO. Therefore, it is a reasonable assumption to think of that bright central spot as a younger ejection of a similar nature to that of knots and inner tips.

A deeper analysis of the nebula's properties and derived magnitudes and its resulting discussion is expected to be found in Masa et al. (in prep.).

Author Contributions: Conceptualization, J.A., M.S.-G., V.B., C.S.C. and A.C.-C.; methodology, E.M., J.A., M.S.-G. and V.B.; software, E.M., J.A., M.S.-G. and V.B.; validation, J.A., A.C.-C. and C.S.C.; formal analysis, E.M.; investigation, E.M., J.A. and M.S.-G.; resources, E.M., J.A., M.S.-G., V.B., C.S.C. and A.C.-C.; data curation, J.A. and A.C.-C.; writing—original draft preparation, E.M.; writing—review and editing, E.M., J.A., M.S.-G., V.B., C.S.C. and A.C.-C.; visualization, E.M.; supervision, J.A. and M.S.-G.; project administration, J.A. and V.B.; funding acquisition, J.A., V.B. and C.S.C. All authors have read and agreed to the published version of the manuscript.

Funding: This research is part of the I + D + i projects PID2019-105203GB-C21 and PID2019-105203GB-C22 founded by Spanish AEI (MICIU) grant 10.13039/501100011033.

Data Availability Statement: Data are contained within the article.

Conflicts of Interest: The authors declare no conflicts of interest.

References

1. Alcolea, J.; Neri, R.; Bujarrabal, V. Minkowski's footprint revisited—Planetary nebula formation from a single sudden event? *Astron. Astrophys.* **2007**, *468*, L41–L44. [CrossRef]
2. Blackman, E.G.; Lucchini, S. Using kinematic properties of pre-planetary nebulae to constrain engine paradigms. *Mon. Not. R. Astron. Soc. Lett.* **2014**, *440*, L16–L20. [CrossRef]
3. Jones, D.; Boffin, H.M.J. Binary stars as the key to understanding planetary nebulae. *Nat. Astron.* **2017**, *1*, 0117. [CrossRef]
4. Douchin, D.; De Marco, O.; Frew, D.J.; Jacoby, G.H.; Jasniewicz, G.; Fitzgerald, M.; Passy, J.C.; Harmer, D.; Hillwig, T.; Moe, M. The binary fraction of planetary nebula central stars—II. A larger sample and improved technique for the infrared excess search. *Mon. Not. R. Astron. Soc.* **2015**, *448*, 3132–3155. [CrossRef]
5. Sánchez Contreras, C.; Alcolea, J.; Bujarrabal, V.; Castro-Carrizo, A.; Velilla Prieto, L.; Santander-García, M.; Quintana-Lacaci, G.; Cernicharo, J. Through the magnifying glass: ALMA acute viewing of the intricate nebular architecture of OH 231.8+4.2. *Astron. Astrophys.* **2018**, *618*, A164. [CrossRef]
6. Sánchez Contreras, C.; Sahai, R.; Gil de Paz, A.; Goodrich, R. Echelle Long-Slit Optical Spectroscopy of Evolved Stars. *Astrophys. J. Suppl. Ser.* **2008**, *179*, 166–194. [CrossRef]
7. Alcolea, J.; Agúndez, M.; Bujarrabal, V.; Castro-Carrizo, A.; Desmurs, J.F.; Martínez-Fernández, J.E.; Sánchez Contreras, C.; Santander-García, M. M 1-92 Revisited: New Findings and Open Questions: New NOEMA Observations of Minkowski's Footprint. *Galaxies* **2022**, *10*, 47. [CrossRef]
8. Bujarrabal, V.; Alcolea, J.; Neri, R. The Structure and Dynamics of the Proto-Planetary Nebula M1-92. *Astrophys. J.* **1998**, *504*, 915–920. [CrossRef]

9. Palmer, J.W.; Lopez, J.A.; Meaburn, J.; Lloyd, H.M. The kinematics and morphology of the planetary nebula Fleming 1. Bullets, jets and an expanding ring. *Astron. Astrophys.* **1996**, *307*, 225.
10. Ohlmann, S.T.; Röpke, F.K.; Pakmor, R.; Springel, V. Hydrodynamic Moving-mesh Simulations of the Common Envelope Phase in Binary Stellar Systems. *Astrophys. J. Lett.* **2016**, *816*, L9. [CrossRef]
11. Solf, J. Long-slit spectroscopic study of the bipolar reflection nebula M 1-92: Detection of compact Herbig-Haro condensations in the lobes. *Astron. Astrophys.* **1994**, *282*, 567–585.
12. Bujarrabal, V.; Alcolea, J.; Sahai, R.; Zamorano, J.; Zijlstra, A.A. The shock structure in the protoplanetary nebula M1-92: Imaging of atomic and H_2 line emission. *Astron. Astrophys.* **1998**, *331*, 361–371.
13. Davis, C.J.; Smith, M.D.; Gledhill, T.M.; Varricatt, W.P. Near-infrared echelle spectroscopy of protoplanetary nebulae: Probing the fast wind in H_2. *Mon. Not. R. Astron. Soc.* **2005**, *360*, 104–118. [CrossRef]
14. Sánchez Contreras, C.; Bujarrabal, V.; Castro-Carrizo, A.; Alcolea, J.; Sargent, A. 1″ Resolution Mapping of the Molecular Envelope of the Protoplanetary Nebula CRL 618. *Astrophys. J.* **2004**, *617*, 1142–1156. [CrossRef]
15. Cox, P.; Lucas, R.; Huggins, P.J.; Forveille, T.; Bachiller, R.; Guilloteau, S.; Maillard, J.P.; Omont, A. Multiple molecular outflows in AFGL 2688. *Astron. Astrophys.* **2000**, *353*, L25–L28.
16. Alcolea, J.; Agúndez, M.; Bujarrabal, V.; Castro Carrizo, A.; Desmurs, J.F.; Sánchez-Contreras, C.; Santander-García, M. M 1-92 revisited: The chemistry of a common envelope nebula? *Proc. Int. Astron. Union* **2018**, *343*, 343–344. [CrossRef]
17. Bujarrabal, V.; Alcolea, J.; Neri, R.; Grewing, M. The mass and temperature distribution in the protoplanetary nebula M 1-92: ^{13}CO interferometric observations. *Astron. Astrophys.* **1997**, *320*, 540–552.
18. Steffen, W.; Koning, N.; Wenger, S.; Morisset, C.; Magnor, M. Shape: A 3D Modeling Tool for Astrophysics. *IEEE Trans. Vis. Comput. Graph.* **2011**, *17*, 454–465. [CrossRef]
19. Santander-García, M.; Bujarrabal, V.; Koning, N.; Steffen, W. SHAPEMOL: A 3D code for calculating CO line emission in planetary and protoplanetary nebulae. Detailed model-fitting of the complex nebula NGC 6302. *Astron. Astrophys.* **2015**, *573*, A56. [CrossRef]
20. Castor, J.I. Spectral line formation in Wolf-Rayet envelopes. *Mon. Not. R. Astron. Soc.* **1970**, *149*, 111. [CrossRef]
21. De Nutte, R.; Decin, L.; Olofsson, H.; Lombaert, R.; de Koter, A.; Karakas, A.; Milam, S.; Ramstedt, S.; Stancliffe, R.J.; Homan, W.; et al. Nucleosynthesis in AGB stars traced by oxygen isotopic ratios. I. Determining the stellar initial mass by means of the ^{17}O/^{18}O ratio. *Astron. Astrophys.* **2017**, *600*, A71. [CrossRef]
22. Karakas, A.I. Helium enrichment and carbon-star production in metal-rich populations. *Mon. Not. R. Astron. Soc.* **2014**, *445*, 347–358. [CrossRef]
23. Cristallo, S.; Piersanti, L.; Straniero, O.; Gallino, R.; Domínguez, I.; Abia, C.; Di Rico, G.; Quintini, M.; Bisterzo, S. Evolution, Nucleosynthesis, and Yields of Low-mass Asymptotic Giant Branch Stars at Different Metallicities. II. The FRUITY Database. *Astrophys. J. Suppl. Ser.* **2011**, *197*, 17. [CrossRef]
24. Stancliffe, R.J.; Tout, C.A.; Pols, O.R. Deep dredge-up in intermediate-mass thermally pulsing asymptotic giant branch stars. *Mon. Not. R. Astron. Soc.* **2004**, *352*, 984–992. [CrossRef]
25. Groenewegen, M.A.T.; van den Hoek, L.B.; de Jong, T. The evolution of galactic carbon stars. *Astron. Astrophys.* **1995**, *293*, 381–395.
26. Marigo, P.; Cummings, J.D.; Curtis, J.L.; Kalirai, J.; Chen, Y.; Tremblay, P.E.; Ramirez-Ruiz, E.; Bergeron, P.; Bladh, S.; Bressan, A.; et al. Carbon star formation as seen through the non-monotonic initial-final mass relation. *Nat. Astron.* **2020**, *4*, 1102–1110. [CrossRef]
27. Pardo, J.R.; Cernicharo, J. Molecular Abundances in CRL 618. *Astrophys. J.* **2007**, *654*, 978–987. [CrossRef]
28. Zhang, Y.; Kwok, S.; Nakashima, J.I.; Chau, W.; Dinh-V-Trung. A Molecular Line Survey of the Carbon-rich Protoplanetary Nebula AFGL 2688 in the 3 mm and 1.3 mm Windows. *Astrophys. J.* **2013**, *773*, 71. [CrossRef]